Geometric stabilization of the electrostatic ion-temperature-gradient driven instability. II. Non-axisymmetric systems

A. Zocco G. Plunk P. Xanthopoulos

Max-Planck-Institut für Plasmaphysik, D-17491, Greifswald, Germany

(Dated:)

Abstract

A non-perturbative analysis for the study non-axisymmetric ($3D$) effects on the linear ion-temperature-gradient (ITG) driven mode is introduced. Perturbations and equilibria are considered to be global on the flux surface, and yet radially local. The analysis is valid for systems arbitrarily far from axisymmetry. It is found that finite Larmor radius (FLR) effects can suppress the global (on the surface) instability, in analogy with the local analysis, but shift its poloidal location from the position of the greatest local instability. Fourier spectra of the instability whose width grows for increasingly non-axisymmetric systems are predicted. Results are in qualitative agreement with numerical global (on the surface) gyrokinetic simulations.

I. INTRODUCTION

The ion-temperature-gradient (ITG) driven instability [1, 2], is one of the major responsible drivers of turbulent losses in modern fusion devices. In stellarators, Xanthopoulos et al. have shown the inherent stabilizing effect of $3D$ geometry on ITG driven turbulence [3]. This stabilization, for small $\rho_* \propto \rho_i/a$, where ρ_i is the ion Larmor radius and a is a macroscopic scale, is partly due to an averaging effect of fluctuations over the full flux surface. For small but finite ρ_*, turbulence reduction occurs due to the suppression of large eddies at scales comparable to those represented by the magnetic geometry itself which can only be captured with a global (at least on the flux surface) gyrokinetic theory, and can only be numerically simulated with a code adapted for this purpose. These purely linear effects govern turbulent activity, and understanding them, along side nonlinear effects such as zonal flows, etc, can be considered as a critically important step toward forming a full picture of the turbulence.

Analytical theories of the ITG instability are mostly based, to leading order, on the radial local approximation, if one excludes the work of Romanelli and Zonca [4], in which the radial structure of the ITG was derived for the first time, and subsequent works [5–7]. All these analysis were concerned with axisymmetric systems, thus focusing on the global features of density and temperature radial profiles, but neglecting the effect of the non-axisymmetric variation of the equilibrium magnetic field on a flux surface. In a stellarator context, the latter effects arise – and are observed to be important [3]. The analytical treatment of surface-global effects was put forth in Ref. [8]. However, the authors considered nearly axisymmetric systems, and presented an asymptotic theory of the global (on the surface) ITG stabilization which is valid only for $\epsilon_h \ll 1$, where ϵ_h is a parameter that measures the deviation from axisymmetry.

In the case of stellarators, a non-asymptotic approach is more realistic and constitutes the aim of this article. Such approach is required since the $3D$ features of stellarators are generally not mere perturbative corrections to tokamaks. We cast the original model equation proposed in Ref. [8] as an eigenvalue problem. This generates a lattice equation for the electrostatic potential similar to the central equation for the wave function of electrons in a crystal [9]. The system of equations is studied both numerically and analytically. We find a residual difference in the growth rate between the local most unstable mode and the

surface global mode, even in the limit of $\rho_* \to 0$. Finite$-\rho_*$ effects can suppress the global (on the surface) instability, and eigenfunctions are found to be localized off the position where the magnetic drift has a local maximum. The results are corroborated by surface global gyrokinetic simulations.

II. LATTICE DRIFT-MODEL

We begin by considering a minimal model for nearly axisymmetric global (on the magnetic surface) ITG modes in the strong interchange regime [8]

$$\left\{\tau - \frac{v_{thi}}{4L_T\omega}g(y)\left(-i\rho_*\partial_y\right)^3\right\}\varphi(y) = -\frac{v_{thi}^2 f\left(y\right)}{\omega^2 L_B L_T}\left(-i\rho_*\partial_y\right)^2\varphi(y), \tag{1}$$

where $\tau = T_{0i}/T_{0e}$, $v_{thi} = \sqrt{2T_{0i}/m_i}$, with T_{0s} the equilibrium temperature for the species s, ω the mode frequency. Here, $y = \alpha/\iota$, α is a field-line label, and ι is the rotational transform. The scale L_B and $L_T^{-1} = (aB_0)d\log T_{0i}/d\psi$ are introduced so that the driving of the toroidal branch of the ITG is

$$\omega_d\omega_T = f(y)\frac{\rho_*^2}{L_T L_B}v_{thi}^2\partial_y^2, \tag{2}$$

where

$$f(y) = -\frac{L_B a}{2}\partial_\psi B \tag{3}$$

and g are $2\pi-$periodic functions, $\rho_* \equiv \iota^{-1}\rho_i = \iota^{-1}v_{thi}/(\Omega_i a)$, $\Omega_i = ZeB_0/m_i$. The scale a characterizes the small scale variation of the equilibrium magnetic field which causes the y dependence of the magnetic drift frequency, $\omega_d \propto f(y)$ [8]. The scales $L_B \sim a$ is expected to be a fraction of the major radius of the device. We neglect radial wave-number effects.

Equation (1) is in many aspects similar to the local eigenvalue ITG equation formulated by using the conventional ballooning transform [10, 11]. However, some important differences need to be explained. First of all, we are considering the toroidal branch of the instability, thus neglecting a quadratic term in $k_\parallel v_{thi}/\omega$, where $k_\parallel$ is the component of the wave vector parallel to the equilibrium magnetic field. This, in ballooning space, would generate a second order derivative which would compel us to solve, for finite global shear, a differential problem in the field-line-following variable. Instead, here we are focusing on the field-line-label dependence of the magnetic drift, that is the dependence on $\alpha = \iota\theta - \phi$, where

$\iota = \mathbf{B}\cdot\nabla\theta/\mathbf{B}\cdot\nabla\phi$ is the rotational transform, and θ and ϕ are the poloidal and toroidal angle-like variables (in magnetic flux co-ordinates). The dependence of the magnetic drift on α makes the coefficients in Eq. (1) non-constant and forces us to consider a differential equation in α. This defines our variable $y = \alpha/\iota$, where we are considering a specific toroidal location, since we are not solving the differential problem along the field line. This does not imply that the mode we are considering is exactly constant along the field line. It simply means that our object of study is a type of mode which varies slowly enough for its structure along the filed line to be neglected. A complete theory of ballooning modes in 3D equilibria is available and was developed by Dewar and Glasser [12]. This proved useful in the study of the ballooning spectrum in stellarators [13]. After solving for the problem along the field line, the remaining 2D problem (in general 3D equilibria), can be solved by using WKB techniques or in analogy with problems in wave propagation in slowly/weakly varying media. The study of the full structure of the mode is therefore possible, but goes beyond the purpose of this article and will not be pursued in our present work.

To extend our analysis of Ref. [8], we first notice that the function $f(y)$ is bounded and periodic on a finite domain $[0, 2\pi]$. For all practical purposes, we can use

$$f(y) = f_0 + \epsilon_h \sum_{k=0}^{K} \left\{ f_k^c \cos ky + f_k^s \sin ky \right\}, \tag{4}$$

where K is a finite integer, f_0, and $f_k^{c,s}$ are some constants, and ϵ_h is a real quantity that measures the "amount of $3D-$ness". The functions g can also be modelled following the prescription of Eq. (4), however we set $g(y) = g' = const \equiv 1$ for simplicity. We now select two representative elements of the series in Eq. (4) (one even and one odd), and proceed with our analysis.

Thus, we have

$$\left[\tau - \frac{v_{thi}}{4L_T\omega}\left(-i\rho_*\partial_y\right)^3\right]\varphi(y) = -\left\{1 + \epsilon_h\left[f_N^c\cos Ny + f_N^s \sin Ny\right]\right\}\frac{v_{thi}^2\left(-i\rho_*\partial_y\right)^2}{\omega^2 L_B L_T}\varphi(y), \tag{5}$$

where N is an order one integer. Notice that φ satisfies periodic boundary conditions, whereas the field-line-following problem requires $\varphi \to 0$ for $\theta \to \pm\infty$, if θ is indeed used to parametrize the field-line-following variable. Equation (5) can be seen as a simplified version of Eq. (17) of Nunami, Watanabe and Sugama [14]. Due to the specification of the magnetic drift frequency through the function $f = 1 + \epsilon_h\left[f_M^c\cos Ny + f_M^s \sin Ny\right]$, we can study global effects for finite ϵ_h, as opposed to what done in Ref. [8], where f was kept

general, but an asymptotic analysis for $\epsilon_h \ll 1$ was performed. When ϵ_h is arbitrary, we resort to a discrete description of the problem. We Fourier expand Eq. (5) [see Appendix A for details] and obtain

$$\begin{aligned}\left(\tau - \frac{1}{4}\frac{v_{thi}/L_T}{\omega} m^3 \rho_*^3\right) \varphi_m = -\frac{v_{thi}^2}{\omega^2 L_B L_T} \rho_*^2 \times \{ m^2 \varphi_m + \\ \frac{\epsilon_h}{2} f_N^c \left[(m-N)^2 \varphi_{m-N} + (m+N)^2 \varphi_{m+N}\right] \\ \frac{\epsilon_h}{2i} f_N^s \left[(m-N)^2 \varphi_{m-N} - (m+N)^2 \varphi_{m+N}\right] \Big\}.\end{aligned} \tag{6}$$

Our original model now shows the remarkable property of being described by a lattice equation for the Fourier components of the eigenfunction. We want to stress that the treatment adopted is very close to what a surface gyrokinetic code actually does. In particular, the number of modes required to consider a surface calculation resolved is related to ρ_*. Before embarking on the study of Eq. (6), we discuss some properties of Eq. (5) and (6) without finite Larmor radius corrections. This is necessary to create contact with previous [8] and new analytic results and to shade light on possible issues related to discretization associated with the surface-global treatment of gyrokinetics, like the emergence of spurious instabilities.

A. No Larmor radius effects

Let us consider Eq. (5) with no FLR terms:

$$\hat{\omega}^2 \varphi(y) = -\left\{1 + \epsilon_h \cos y\right\} \left(-i\rho_* \partial_y\right)^2 \varphi(y), \tag{7}$$

where $\hat{\omega} = \omega/(v_{thi}/\sqrt{\tau L_T L_B})$. For the case $\epsilon_h \geq 1$, we observe that the coefficient of the derivative term has zeros, making the equation singular. These singularities, however, are not essential and Fuchs theorem guarantees that a local solution can always be found in the neighborhood of y_0 such that $1 + \epsilon_h \cos y_0 = 0$. For the specific case of Eq. (7), for $y \approx y_0$, we have

$$\rho_*^2 \partial_y^2 \varphi \approx \frac{\hat{\omega}^2}{(y - y_0)\epsilon_h \sin y_0} \varphi. \tag{8}$$

By introducing the Frobenius series $\varphi = (y - y_0) \sum_{k=0}^{\infty} c_k (y - y_0)^k$, it is easy to derive the recursive relation for its coefficients

$$c_k = \frac{(-1)^k}{(k+1)\,(k!)^2} \left(\frac{\hat{\omega}^2}{\rho_*^2 \epsilon_h \sin y_0}\right)^k c_0,$$

which gives

$$\varphi(y) \approx \sqrt{y-y_0} J_1\left(2\frac{\hat{\omega}}{\rho_* \sqrt{\epsilon_h \sin y_0}}\sqrt{y-y_0}\right), \quad \text{for } y \approx y_0 \tag{9}$$

where J_n is the Bessel function of integer order. Thus, φ is regular and changes sign at $y = y_0$, but no statement can be made on whether the solution of the full problem, with periodic boundary conditions, has only zeros that coincide with the zeros of the function $1 + \epsilon_h \cos y$. In fact, by just inspecting Eq. (7) we see that if y_0 is a zero of φ, the LHS is identically zero, and the RHS can be zero if $\partial_y^2 \varphi(y_0) = 0$, for any non-zero value of $1 + \epsilon_h \cos y_0$. On the other hand, when $1 + \epsilon_h \cos y$ has no zeros, the eigenfunction φ has an arbitrary number of zeros! This can be seen in the following way.

When ϵ_h is small but finite, insofar the coefficient of the derivative term of Eq. (5) is not zero, the WKB analysis of Ref. [8] can still be performed. Let us return momentarily to the more general form, i.e. we consider $1 + \epsilon_h \cos y \to h_{\epsilon_h}(y)$ in Eq. (7). We introduce $\varphi = \exp[s(y)/\rho_*]$, to obtain, in the limit $\rho_* \to 0$, $s'(y) = \pm\hat{\omega}/h_{\epsilon_h}^{1/2}(y)$, where $\hat{\omega} = \omega/(v_{thi}/\sqrt{L_B L_T \tau})$. The approximate WKB solution is then $\varphi \propto \exp\{\hat{\omega}/\rho_* \int^y d\eta h_{\epsilon_h}^{-1/2}(\eta)\}$, which is $2\pi-$periodic only if

$$\omega = \pm i \frac{m_0 \rho_*}{\oint \frac{d\eta}{\sqrt{h_{\epsilon_h}(\eta)}}} \frac{v_{thi}}{\sqrt{L_B L_T \tau}}, \tag{10}$$

where m_0 is an integer and $\oint(\cdots) = (2\pi)^{-1}\int_{\eta_0}^{\eta_0+2\pi} d\eta$, $\forall\ \eta_0$. We now have, for $h_{\epsilon_h}(y) = 1 + \epsilon_h \cos y$,

$$\varphi_{WKB} \propto \exp\left[i\pi m_0 \frac{F\left(\frac{y}{2}, \frac{2\epsilon}{1+\epsilon}\right)}{K\left(\frac{2\epsilon}{1+\epsilon}\right)}\right] \tag{11}$$

where F and K are the elliptic integrals of the first kind (incomplete and complete). The number of zeros of this eigenfunction is fixed by the arbitrary quantum number $m_0 \sim \rho_*^{-1} \gg 1$. This eigenfunction is plotted in Fig. (1). Here we observe that the mode has a localization at the location where the magnetic drift has a minimum.

B. Properties of the discrete spectrum: no FLR

We now discuss what are the limitations of a discrete representation for surface-global effects in gyrokinetics. We find convenient to write Eq. (6) in the following way

$$A_{nm}\varphi_m = 0, \tag{12}$$

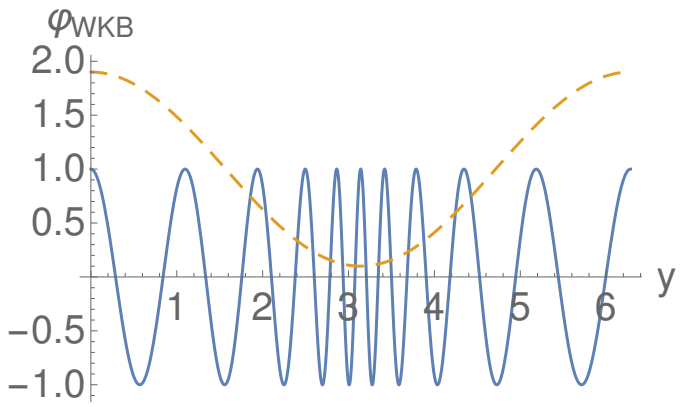

Figure 1: Eigenfunction from the WKB approximation Eq. (11) (solid line) for $m_0 = 10$ and $\epsilon_h = 0.9$. The dashed line is the function $h_{\epsilon_h} = 1 + \epsilon_h \cos(y)$. A localization at the minimum of h_{ϵ_h} is observed.

with

$$A_{nm} = \begin{bmatrix} \ddots & 4\,(f_N^c + i f_N^s) & & & & & & \\ 9\,(f_N^c - i f_N^s) & a_{-2} & 1\,(f_N^c + i f_N^s) & & & & & \\ & 4\,(f_N^c - i f_N^s) & a_{-1}(\omega) & 0 & & & & \\ & & 1\,(f_N^c - i f_N^s) & a_0(\omega) & 1\,(f_N^c + i f_N^s) & & & \\ & & & 0 & a_1(\omega) & 4\,(f_N^c + i f_N^s) & & \\ & & & & 1\,(f_N^c - i f_N^s) & a_2(\omega) & 9\,(f_N^c + i f_N^s) & \\ & & & & & 4\,(f_N^c - i f_N^s) & \ddots & \end{bmatrix}, \tag{13}$$

and $a_m(\omega) = \left(\tau + \frac{v_{thi}^2}{\omega^2 L_B L_T} m^2 \rho_*^2\right) \frac{2}{\epsilon_h} \frac{\omega^2}{v_{thi}^2/(L_B L_T)\rho_*^2} = \mathcal{O}(\rho_*^{-2})$, where we are not specifying the matrix size yet.

The global eigenvalue is therefore the solution of

$$\det A_{nm} = 0. \tag{14}$$

Equation (14) determines, for *any* ϵ_h, the global eigenvalue we are looking for. Notice that the number of roots of Eq. (14) depends on the size of the matrix A, and we have no knowledge, a priori, on which is the most unstable mode. In fact, the choice of the acceptable roots which we can consider true eigenvalues of the original continuous problem is not a trivial task.

We prove the relation between the discrete description and the analytical solution (11). Thus we take, in Eq. (6) $f^c_N = 1$, $f^s_N = 0$, and $N = 1$, to obtain

$$\left[\hat{\omega}^2\delta_{nm} + \rho_*^2 B_{nm}(M,\epsilon_h) - \frac{\hat{\omega}}{4}\sqrt{\frac{L_B}{L_T\tau}}\rho_*^3 G_{nm}(M)\right]\varphi_m = 0, \tag{15}$$

where δ_{nm} is the identity matrix,

$$B_{nm}(M,\epsilon_h) = \begin{bmatrix} \ddots & 4\frac{\epsilon_h}{2} & & & & & & \\ 9\frac{\epsilon_h}{2} & 4 & 1\frac{\epsilon_h}{2} & & & & & \\ & 4\frac{\epsilon_h}{2} & 1 & 0 & & & & \\ & & 1\frac{\epsilon_h}{2} & 0 & 1\frac{\epsilon_h}{2} & & & \\ & & & 0 & 1 & 4\frac{\epsilon_h}{2} & & \\ & & & & 1\frac{\epsilon_h}{2} & 4 & 9\frac{\epsilon_h}{2} & \\ & & & & & 4\frac{\epsilon_h}{2} & \ddots & \end{bmatrix} \tag{16}$$

represents the tridiagonal matrix arising from the operator $[1+\epsilon_h\cos(y)]\partial_y^2$,

$$G_{nm}(M) = \begin{bmatrix} \ddots & & & & & & & \\ & -8 & & & & & & \\ & & -1 & 0 & & & & \\ & & & 0 & & & & \\ & & & 0 & 1 & & & \\ & & & & & 8 & & \\ & & & & & & \ddots & \end{bmatrix} \tag{17}$$

is the diagonal matrix due to ∂_y^3, and $-M < m < M$, with $M \gg 1$. All matrices are $(2M+1)\times(2M+1)$. The matrix B_{nm} has $N_m = 3M-2$ non-zero entries. The FLR correction has been left and it will be discussed in the next Section, but it is not essential for now. Equation (15) can be recast as an eigenvalue problem by writing $\hat{\omega}^2\delta_{nm} = \hat{\omega}\delta_{nm}\hat{\omega}\delta_{nm}$, and completing the square for the unknown $\hat{\omega}\delta_{nm}$. The result is

$$\hat{\omega}_{(M)}\delta_{nm}\varphi_m = \left\{\frac{1}{8}\sqrt{\frac{L_B}{L_T\tau}}\rho_*^3 G_{nm}(M) \pm \left[\frac{1}{64}\frac{L_B}{L_T\tau}\rho_*^6 G_{nm}^2(M) - \rho_*^2 B_{nm}(M,\epsilon_h)\right]^{1/2}\right\}\varphi_m. \tag{18}$$

The solutions $\hat{\omega}_{(M)}$ are then obtained as the eigenvalue of the matrix in the curly brackets. The number of eigenvalues is, of course, a function of the dimension of the problem, M.

Of all these eigenvalues, from the point of view of the stability of the system, the most interesting are those with largest imaginary part, that is, the most unstable ones. When the G_{mn} (FLR) terms of Eq. (18) are neglected [18], and the eigenvalue problem to solve is

$$\det\left[iB_{mn}^{1/2}(M,\epsilon_h)-\frac{\hat{\omega}}{\rho_*}\delta_{mn}\right]=0, \tag{19}$$

that is, ρ_* can be factorized, and there seem not to be an ultimate most unstable mode. This, of course, could be seen in Eq. (1). The situation is analogous to what happens in the local limit if one neglectes FLR effects, then $\hat{\omega}=ik_y\rho_i$, and indeed the growth rate is an unbounded function of the wavenumber k_y. In the global case, when the dimension of the problem in Eq. (18) grows, the number of eigenvalues grows as $2M+1$. We then find more convenient to solve the following eigenvalue problem

$$\det\left[i\frac{B_{mn}^{1/2}(M,\epsilon_h)}{M}-\frac{\hat{\omega}}{\rho_* M}\delta_{mn}\right]=0. \tag{20}$$

If we want to compare an eigenvalue solution of Eq. (20) with the WKB formula of Eq. (10), we fix the parameters of Eq. (10), m_0, and ρ_*, let us say $m_0=30$, and $\rho_*=0.015$, so that $m_0\rho_*=0.45$. We then select the $j-$th root of Eq. (20) for which $\hat{\omega}_j(\epsilon_h=0.001)/(\rho_* M)=0.45$, (which occurs at $j=90$, for $M=100$, or $j=180$ when $M=200$, and so on) and trace it as a function of ϵ_h. The result is in Fig. (2), where it is compared to Eq. (10), and to its $\epsilon_h\ll 1$ perturbative equivalent of Ref. [8]. The agreement is excellent. For completeness, we plot the eigenfunction obtained from a periodic boundary-value solution of the continuum equation, and the reconstruction from the discrete solution with $M=40$ Fourier harmonics. Results are in Fig. (3) and show no discrepancy between the two solutions.

In this process, for each system size, we are not choosing the eigenvalue with the largest imaginary part, but the one that matches a given WKB eigenvalue for $\epsilon_h\to 0$ for a given $m_0\rho_*$. However, by increasing M, we could always evaluate which one is the most unstable $j-$th eigenvalue of the $2M+1$ evaluated. If we create a sequence of such most unstable modes ordered by increasing $\hat{\gamma}=\Im[\hat{\omega}]$, for a given ρ_*, we can also select the j for which $\hat{\omega}_j(\epsilon\to 0)$ is equal to a given $m_0\rho_*$. Let us progressively increase the dimension of Eq. (19), and find, for each iteration, the $j-$th eigenvalue with the largest imaginary part at $\epsilon_h=0.001$. When $M=m_0=30$, we then trace this eigenvalue as a function of ϵ_h. The result of this procedure is shown in Fig. 4. Here we observe a surface-global destabilization

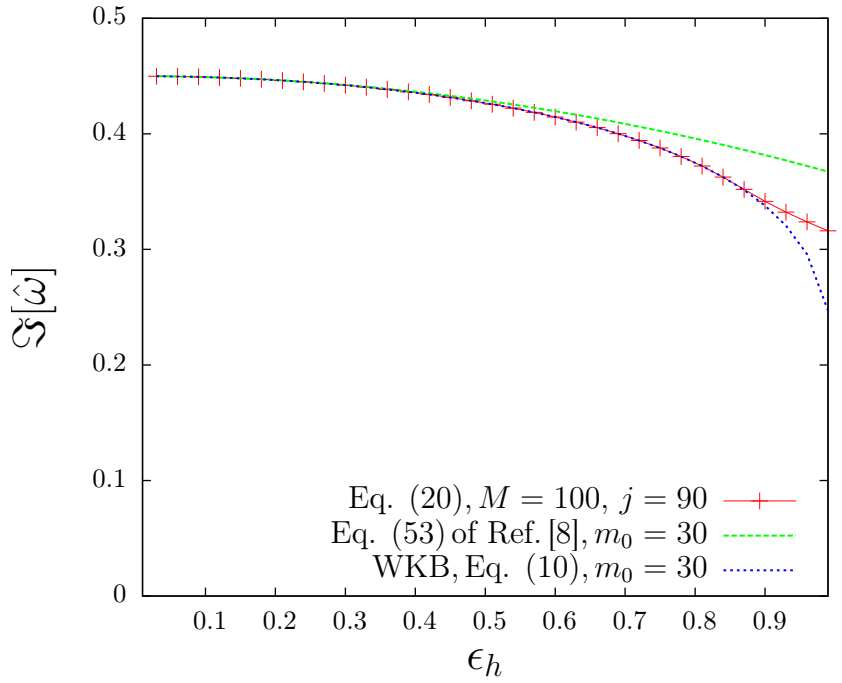

Figure 2: Comparison of the eigenvalue from the WKB solution [Eq. (10)], Eq. (53) of Ref. [8], and the $j-$th solution of (20) for which $\hat{\omega}_j(\epsilon_h = 0.001)/(\rho_* M) = 0.45$. Here $M = 100$, $j = 90$.

which, however, is never enough to make the mode due to the discretization of the global problem more unstable than the local one.

It is possible to derive analytically the properties of the eigenvalues of the matrix $B^{1/2}_{mn}$ which are plotted in Fig. 4. Consider the Fourier expansion of Eq. (7). This is Eq. (6) with $N = 1$, $f^s_N = 0$, $f^c_N = 1$, and $m\rho_* \ll 2\left(\tau L_T/L_B\right)^{1/4}$. By using the centered finite-difference formulas of derivatives, for slowly varying φ_m, we obtain

$$\frac{\partial^2 \varphi_m}{\partial m^2} + \frac{m}{1+m^2}\frac{\partial \varphi_m}{\partial m} = -\frac{1}{2}\left\{1 + \frac{1}{\epsilon_h \rho_*^2}\frac{\hat{\omega}^2 + m^2\rho_*^2}{1+m^2}\right\}\varphi_m, \tag{21}$$

where the continuum approximation will be justified a posteriori.

If, for a given $m_0 \sim \rho_* \gg 1$, we seek an eigenvalue $\hat{\omega}_0^2 \sim m_0^2\rho_*^2(1+\epsilon_h)$, the coefficient on the RHS of Eq. (21) tends to zero. We can then order the derivatives on the LHS small. How small will be evident from the analysis. Let us take $m \approx m_0 - \delta m$, with $m_0 \sim \rho_*^{-1} \gg 1$, $m_0^{-2} \ll \delta m/m_0 \ll 1$ and positive; that is, m_0 will be a maximum of φ_m. Then, if we Taylor expand (21) around m_0, we obtain

$$\frac{\partial^2 \varphi_m}{\partial m^2} + \frac{1}{2}\left(a - bm\right)\varphi_m = 0, \tag{22}$$

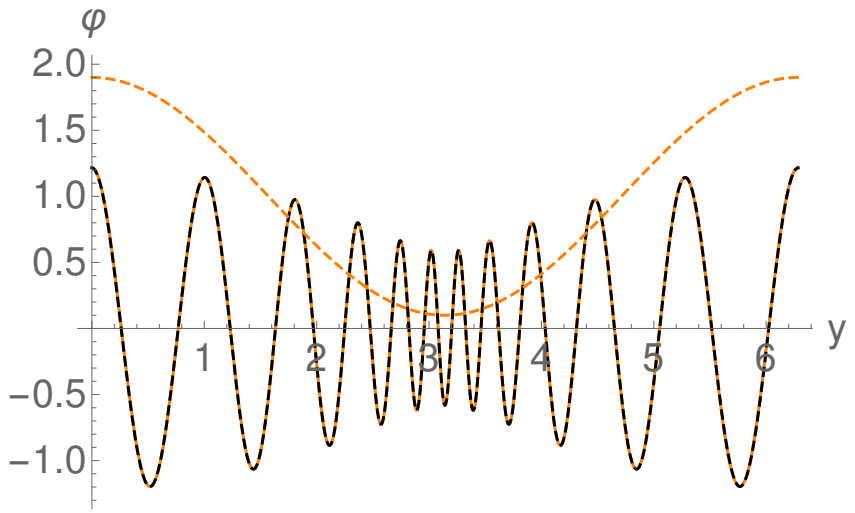

Figure 3: Solution of Eq. (7) as a periodic boundary-value problem (dark dashed line) and from the discrete eigenvalue formulation (light solid line). Here $m_0 = 11$, $\epsilon_h = 0.9$, thus $\hat{\omega}/\rho_* = i11(\pi/2)\sqrt{1.9}/K(1.8/1.9) \approx i8.26$, according to Eq. (10). The number of Fourier harmonics kept is $M = 40$. The light dashed line is the function $1 + \epsilon_h \cos y$.

where $a = 1-[3/(\epsilon_h\rho_*^2 m_0^2)]\,(\hat{\omega}^2 + m_0^2\rho_*^2)+2/\epsilon_h$, and $b = [2/(\epsilon_h\rho_*^2 m_0^2)]\,(\hat{\omega}^2 + m_0^2\rho_*^2)\,[m_0\rho_*^2/(\hat{\omega}^2+ m_0^2\rho_*^2)-2m_0^{-1}] \sim \rho_*$. The solution of this equation that decays for $m \gg 1$ is the Airy function

$$\varphi_m = \varphi_0 Ai\left[\frac{bm - a}{(2b^2)^{1/3}}\right]. \tag{23}$$

We immediately see that $\varphi_m'/\varphi_m \sim b^{1/3} \sim m_0^{-1/3} \sim \rho_*^{1/3} \ll 1$, which justifies the continuum approximation. The eigenfunction defined by Eq. (23) has a maximum at m_0 if

$$bm_0 - a = a_i' \left(2b^2\right)^{1/3}, \tag{24}$$

where a_i' are the zeros of the derivative of the Airy function Ai. Explicitly, this is

$$\frac{\hat{\omega}^2}{m_0^2\rho_*^2} = -\left(1+\epsilon_h\right) - 2\frac{a_i'\epsilon_h}{\left(m_0\epsilon_h\right)^{2/3}}\left[-\left(1 + 2\frac{\hat{\omega}^2}{m_0^2\rho_*^2}\right)\right]^{2/3}, \tag{25}$$

where the second term on the RHS is a global correction to the local non-axisymmetric mode

$$\hat{\omega}_0 = im_0\rho_*\sqrt{1+\epsilon_h}. \tag{26}$$

The correction is stabilizing. Indeed, by writing $\hat{\omega} \approx \hat{\omega}_0 + \delta\hat{\omega}$, with $\delta\hat{\omega} \ll \hat{\omega}_0$, we obtain

$$\delta\hat{\omega} = -i\left(\rho_*\epsilon_h\right)^{2/3}\left(m_0\rho_*\right)^{1/3}\frac{\left(1+2\epsilon_h\right)^{2/3}}{\left(1+\epsilon_h\right)^{1/2}}\left|a_i'\right|. \tag{27}$$

We now compare the solution of the eigenvalue equation derived by using the continuum approximation of the Fourier series expansion, Eq. (25) with $a_i' = -1.01879$, with the eigenvalues of $B_{mn}^{1/2}$ with largest imaginary part. The results are in Fig (5). The agreement is remarkable, and it improves for $\rho_* \to 0$, $M \to \infty$, keeping $\rho_* M$ constant. We conclude that Eq. (25) is the correct eigenvalue equation that predicts surface-global effects on the most unstable local non-axisymmetric mode without FLR corrections.

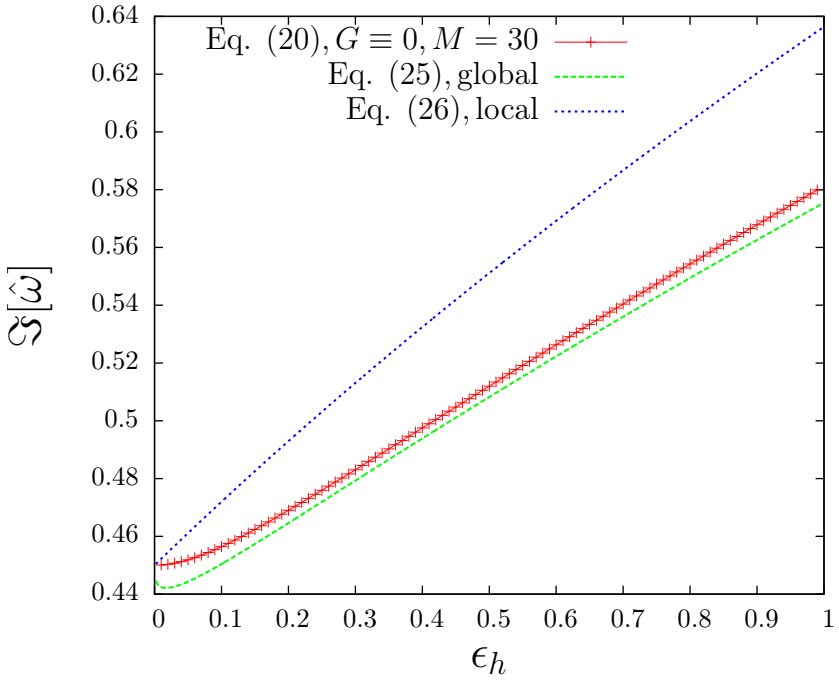

Figure 4: Most unstable eigenvalue (crosses), solution of Eq. (20) for $M = 30$, $\rho_* = 0.015$. Solution of Eq. (25), derived from the continuum approximation of the discrete Fourier expansion of Eq. (7) when $m_0 = M = 30$. The local non-axisymmetric mode Eq. (26).

The relation between the WKB and the discrete treatment of the problem is becoming evident. The global correction to the magnetic drift, $1 + \epsilon_h \cos y$, is causing the formation of small scales due to the localization of the eigenfunction at the minima of the magnetic drift [See Fig. (3)]. The resolution of these structures requires to consider modes that are more and more unstable, the larger is the system size. Such modes can be seen as finite$-\rho_*$ corrections to local non-axisymmetric modes [see Eq. (25)]. In the next section we show that finite Larmor radius effects can regularize these modes.

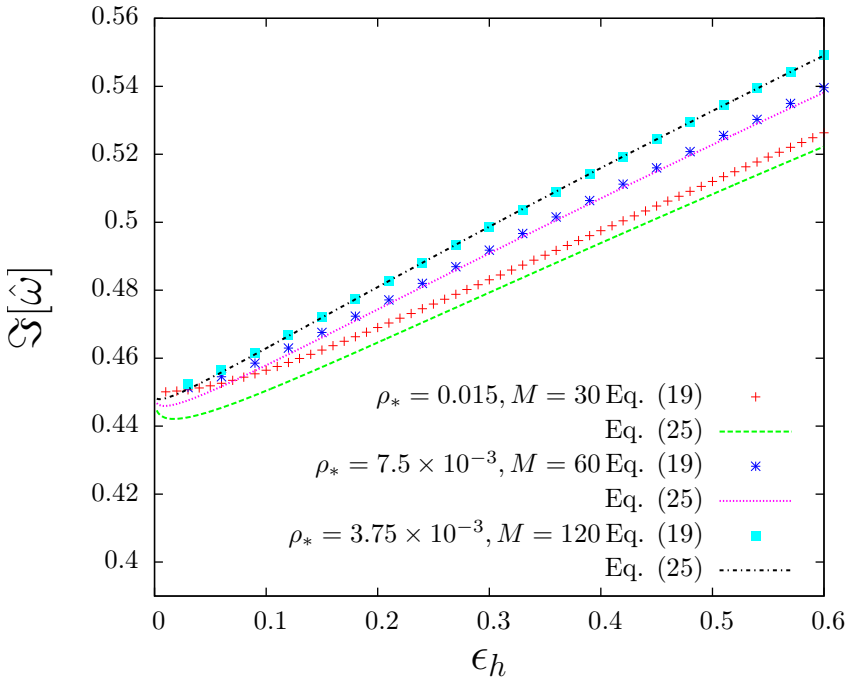

Figure 5: Comparison of the eigenvalues derived from the discrete representation [Eq. (19)] and from the continuum approximation [Eq. (25)]. Here $m_0 = M = (30, 60, 120)$ and $\rho_* = (0.015, 0.0075, 0.00375)$. The product $M\rho_*$ is kept constant. The agreement improves for larger system size (larger M).

C. Larmor Radius Effects

When finite Larmor radius effects are included, we expect a maximum growth rate that needs to be compared to the maximum local one. This is evaluated from Eq. (5) by taking a costant magnetic drift equal to the maximum of $1 + \epsilon_h \cos y \equiv 1 + \epsilon_h$, using $\varphi \sim \exp[iny]$, and maximazing the eigenvalue obtained over n, yielding

$$\hat{\gamma} = \frac{4}{3^{3/4}} (1 + \epsilon_h)^{3/4} \left(\frac{L_T \tau}{L_B} \right)^{1/4}, \tag{28}$$

at $n_c \rho_* = 2 \left[(4 L_T \tau / 3 L_B)(1 + \epsilon_h) \right]^{1/4}$.

An interesting limit is $\rho_* \to 0$. Scanning in ϵ_h and taking the limit $\rho_* \to 0$, we obtain a residual difference between the local and global maximum growth rates, as shown in Fig. (6). A maximum $M = 38$ is enough to resolve the case for smallest $\rho_* = 0.05$. This requires matrices of $3M - 2 = 74$ dimension to be considered. The global most unstable mode shows a dependence in ϵ_h similar to the local mode for $\epsilon_h \gtrsim 0.4$, and a slow variation

for $\epsilon_h \lesssim 0.4$. We suggest this is associated to the transition from the axisymmetric spectrum of normal modes [Eq. (26)] to a spectrum of globally stabilized nonaxisymmetric modes.

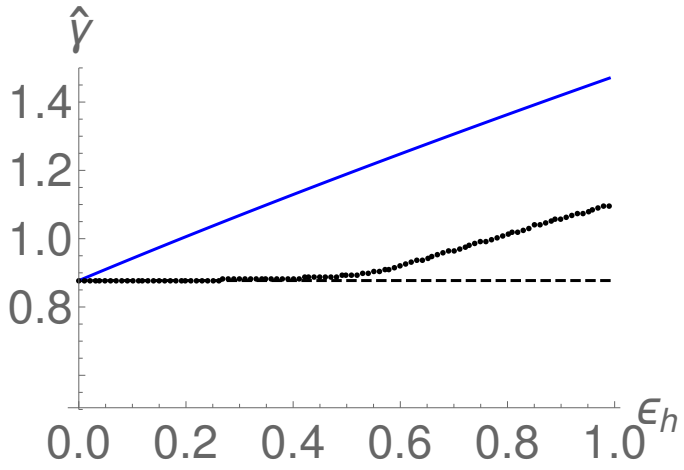

Figure 6: Residual difference between local [Eq. (28), solid line] and global [Eq. (18), dots] maximum growth rates as axisymmetry is approached in the asymptotic limit $\rho_* = .05$. The black dashed line is the local axisymmetric solution given by Eq. (28) with $\epsilon_h = 0$.

This result is more directly related to surface global GENE gyrokinetic simulations [3, 15] if we plot the most unstable growth rate as a function L_B/L_T, which is proportional to the code input parameter a_r/L_T, with a_r an average of the device's minor radius. Results in Fig. (10). The global (surface) mode remains more stable than the maximum local one. For a given value of ϵ_h, a complete stabilization of the global mode can occur at sufficiently large ρ_*, see Fig. (7). It can be verified that $\rho_* = 0.05$ is small enough to consider the solution converged in the sense of Fig. (9).

The presence of the FLR stabilization can be easily understood after inspecting Eq. (18). This is closely related to the local dispersion relation of the toroidal ITG with FLR effects [10, 11]

$$2\omega = \frac{1}{4}k_\alpha^3\rho_i^3\frac{v_{thi}}{L_T\tau} \pm \sqrt{\left(\frac{1}{4}k_\alpha^3\rho_i^3\frac{v_{thi}}{L_T\tau}\right)^2 - \frac{4v_{thi}^2}{L_B L_T\tau}k_\alpha^2\rho_i^2(1+\epsilon_h)}. \tag{29}$$

In fact, Eq. (18) is simply the matrix formulation of Eq. (29) when a whole spectrum of eigenvalues is induced by the periodic inhomogeneous driving term of Eq. (5).

In the limit of $\rho_* m \ll (\tau L_T/L_B)^{1/4}$, the contribution of G_{mn} can be neglected, and a spectrum of unstable modes is found. Therefore, the balance of the terms associated to B_{mn} and G_{mn} sets the maximum global eigenvalue. This occurs for the maximum integer

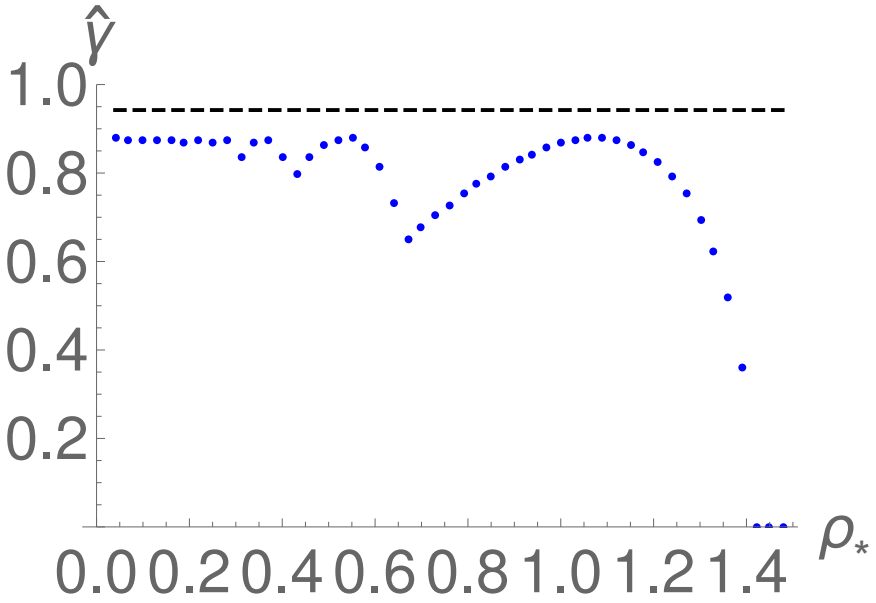

Figure 7: Global vs. local mode as a function of ρ_* for $\epsilon_h = 0.1$. Blue dots represent the maximum growth rate of the global solution, and the black dashed line is the maximum growth rate of the local mode, $\hat{\gamma} = (1+\epsilon_h)^{3/4} 3^{4/3}$.

M below the critical M_c for which

$$\left\| (\rho_*^3 G_{nm})^2 (1/64) L_B / L_T \tau \right\| > \left\| \rho_*^2 B_{nm} \right\|, \tag{30}$$

where $\|A\|$ denotes the norm of a matrix. As Fig. (8) shows, the norms of G_{nm} and B_{nm} are both monotonic growing functions of M with $\partial_M \|G_{nm}^2\| > \partial_M \|B_{nm}\|$. Thus, M_c is only a function of ρ_*, ϵ_h, and L_B/L_T. Figure (9) shows that the most unstable global mode converges for values of $M > M_c$. This is a surface-global variety of the common local FLR stabilization.

The spectrum of φ_m^2 is broader with increasing non-axisymmetry, see Fig (11). The same feature is reproduced by gyrokinetic simulations on the surface, see Fig (12).

Finally, Fig. (13) shows that the mode localizes around specific value of y, which is actually *not* the locally most unstable y=0! This is perhaps the familiar y shift of the "band" observed in GENE simulations [15, 16], due to the tendency of drift waves to propagate in a particular direction. In this case, since the density gradient is zero, the drift wave propagation is due to FLR effects.

From this section we draw some important conclusions: the $y-$variation of the strength

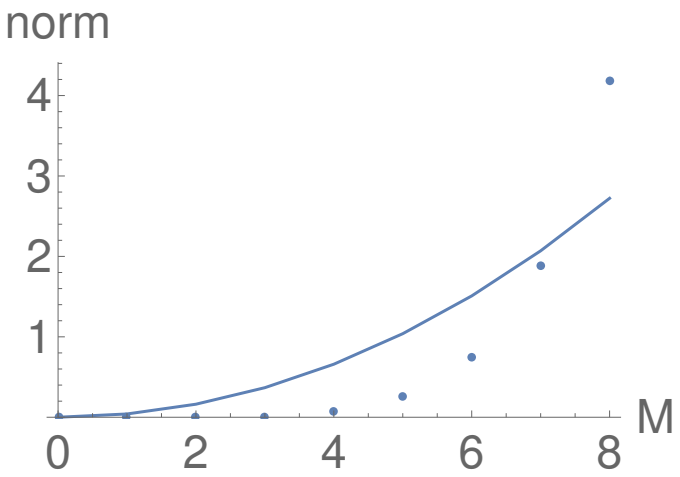

Figure 8: Norms of $\rho_*^2 B_{nm}$ (solid line) and $(\rho_*^3 G_{nm})^2 (1/64) L_B/L_T\tau$ (points) as a function of M, where $(2M+1)\times(2M+1)$ is the dimension of B_{nm} and G_{nm}. Here $L_B/L_T\tau = 2^4$, $\rho_* = .2$, and $\epsilon_h = 0.3$. For $\left\|(\rho_*^3 G_{nm})^2 (1/64) L_B/L_T\tau\right\| > \left\|\rho_*^2 B_{nm}\right\|$, complete FLR stabilization occurs and the upper bound of growth rates is reached.

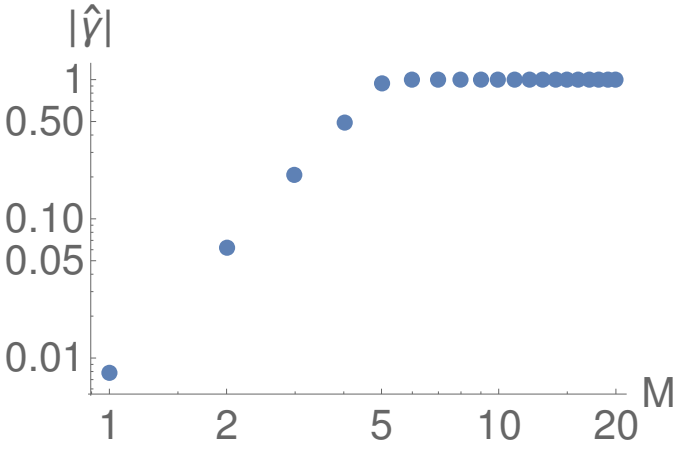

Figure 9: Normalized maximum global growth rate as a function of M, where $(2M+1)\times(2M+1)$ is the matrix dimensions. Here $L_R/L_T\tau = 2^4$, $\rho_* = 0.2$, and $\epsilon_h = 0.3$. Convergences is obtained for $M > M_c$, where M_c is the smallest integer than satisfies the FLR stability condition $\left\|(\rho_*^3 G_{nm})^2 (1/64) L_B/L_T\tau\right\| > \left\|\rho_*^2 B_{nm}\right\|$.

of the magnetic drift is averaged so that a global (surface) mode is less unstable than a local one [Eq. Fig. (6)], global modes show a tendency to rotate [Eq. (18)] in analogy to what FLR effects do to local modes [contributing to stabilization, see Eq. (18)], FLR effects

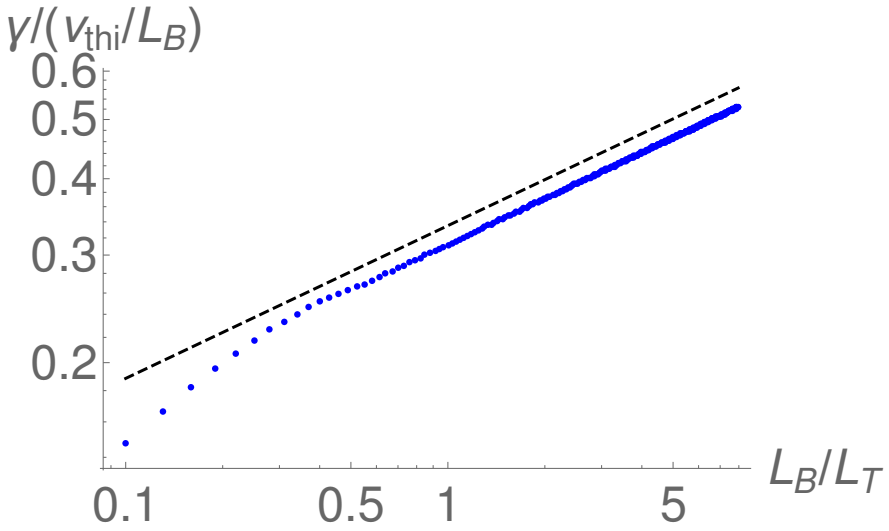

Figure 10: Normalized maximum global growth rate as a function of L_T/L_B. Here $\rho_* = 0.04$, $M = 38$, and $\epsilon_h = 0.1$.

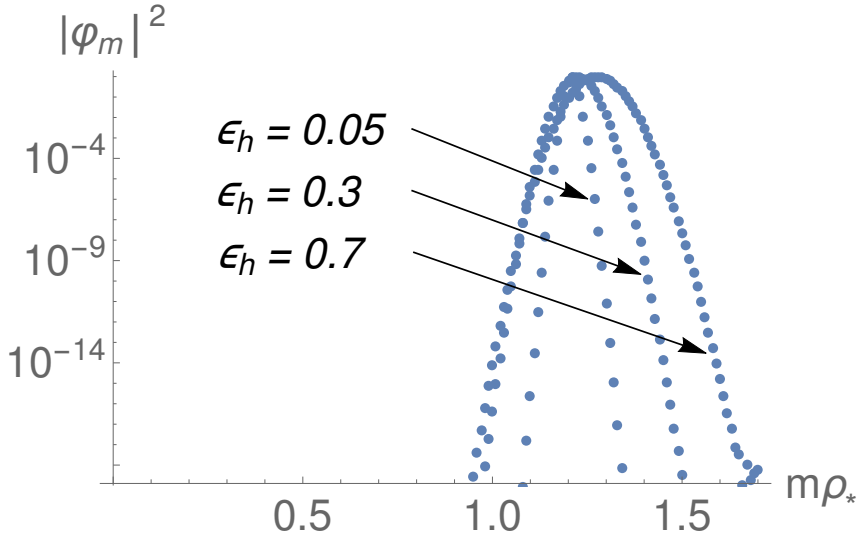

Figure 11: The spectrum of the solution of Eq. (6) for different levels of non-axisymmetry. Here $\rho_* = 0.01$, $L_B/(L_T\tau) = 2^4$, $M_{max} = 170$. A broadening of the width is observed with increasing ϵ_h.

can suppress the global mode [see Fig. (7)], and the global eigenfunction is not localized at the location where the local instability has a maximum. One final remark is on the comparison of the nearly axisymmetric results of Fig. (2) and the non-axisymmetric results of Fig. (6). In the first case, we confirmed the presence of a geometric stabilization for $\epsilon_h < 1$, already derived in Ref. [8] for $\epsilon_h \ll 1$. Here the local growth rate undergoes a global

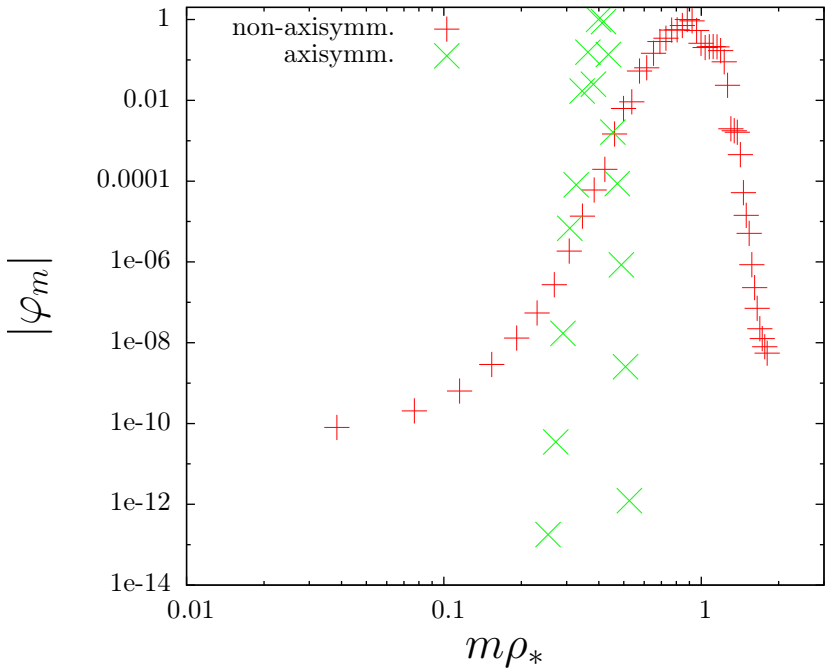

Figure 12: Axisymmetric versus non-axisymmetric (poloidally) global spectra from global (on the surface) GENE simulations.

stabilizing correction, $\hat{\gamma} = m_0\rho_*(1-\mathcal{O}(\epsilon_h^2))$, persistent for $\rho_* \to 0$. For arbitrary ϵ_h, the non-axisymmetric local mode is also stabilized by global effects, but now $\hat{\gamma} = m_0\rho_*(\sqrt{1+\epsilon_h} - \mathcal{O}((\rho_*\epsilon_h)^{2/3}))$. Which type of mode would prevail in a numerical simulation depends on the specific values of ϵ_h and ρ_*. All these features make surface-global effects quite different from radially-global ones.

III. SUMMARY AND DISCUSSION

In this article we extend a previous work on global (surface) effects on ITG modes [8] to the case of fully non-axisymmetric systems.

It has been found that global (on the surface) effects are stabilising for all cases investigated [Figs. (6), (10)]. The spectrum obtained (see Fig. (11)) is consistent with surface gyrokinetic simulations shown in Fig. (12). The mechanism for stabilization is an averaging effect and is analogous to the $\epsilon_h \ll 1$ case of Ref. [8] [Eqs. (10) and (20)]. The present analysis also includes finite Larmor radius (FLR) effects. We found that the global instability can be completely suppressed in this regime [see Fig. (7)], and the localisation of

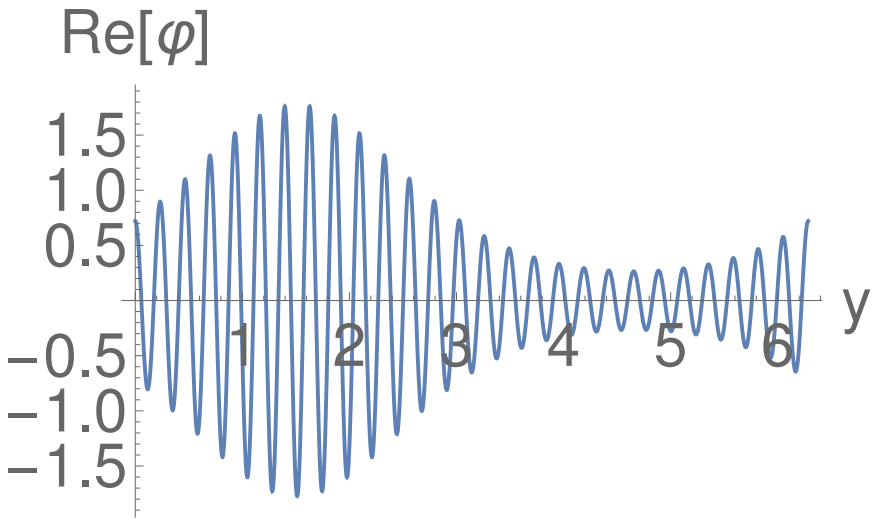

Figure 13: Real part of the most unstable mode solution of the eigenvalue problem (18) for $\rho_* = 0.04$, $M = 100$, and $\epsilon_h = 0.1$. Note that the mode location is shifted relative to the position of greatest local instability, $y = 0$.

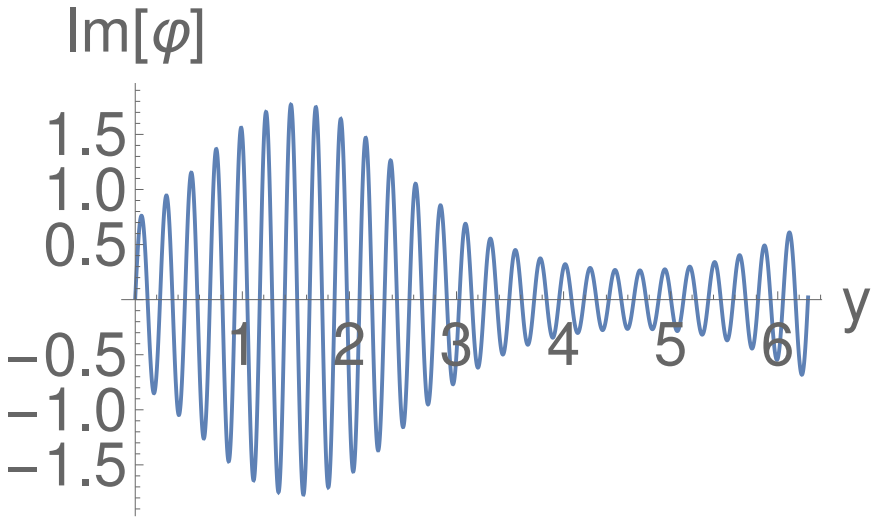

Figure 14: Imaginary part of the most unstable mode solution of the eigenvalue problem (18) for $\rho_* = 0.04$, $M = 100$, and $\epsilon_h = 0.1$. Note that the mode location is shifted relative to the position of greatest local instability, $y = 0$.

the mode is shifted to locations where the curvature drive does not have a maximum, as observed in surface gyrokinetic simulations [3]. This effect is due to the mode propagation associated with the presence of a real frequency, in this case generated by FLR corrections. The dynamics of wave packets is also investigated. When FLR corrections are taken into

consideration, an additional stabilizing ρ_*- effect is identified.

The present results are complementary to a recent nonlinear numerical study by the same authors [3]. Most of the features of the small$-\rho^*$ regime of Xanthopoulos et al. [3] are indeed recovered in our work, specifically: the stabilization of the ITG on the surface, the poloidal (y) offset of the mode from the location of maximum magnetic drift ($y = 0$) due to FLR effects, the broader spectrum of modes for more non-axisymmetric systems.

The analysis has been concerned with normal modes, *i.e.* those which have a single complex frequency ω, determining their global dynamics. However, it may not be the case that such modes survive in fully developed turbulence. In particular, although normal modes have been observed as a key component of the turbulence in flux-tube simulations, the issue is open for the global normal modes arising when larger domains are used. Indeed, it is doubtful that spatial correlation across a magnetic flux surface can be maintained in the nonlinear state when the propagation of a typical drift wave over this distance takes much longer than the nonlinear decorrelation time (in the small ρ_* limit). Thus, a more complete understanding of turbulence properties in a surface-global setting would require to consider an improved linear calculation involving the dynamics of a wave packet, *i.e.* a structure that is localized in space. Indeed, what is observed in turbulence simulations is reminiscent of a wave packet, localized to regions of greater instability [3]. This aspect of the study is left for future work.

Acknowledgments

We thank Per Helander for contributing to a preliminary version of the manuscript. This work has been carried out within the framework of the EUROfusion Consortium and has received funding from the Euratom research and training programme 2014-2018 and 2019-2020 under grant agreement No 633053. The views and opinions expressed herein do not necessarily reflect those of the European Commission.

---

[1] L. I. Rudakov and R. Z. Sagdeev, Dokl. Akad. Nauk CCCP **138**, 581 (1961).

[2] B. Coppi, M. N. Rosenbluth, and R. Z. Sagdeev, Phys. Fluids **10**, 582 (1967).

[3] P. Xanthopoulos, G. G. Plunk, A. Zocco, and P. Helander, Phys. Rev. X **6**, 021033 (2016).

[4] F. Romanelli and F. Zonca, Phys. Fluids B **5**, 4081 (1993).

[5] J. B. Taylor, H. R. Wilson, and J. W. Connor, Plasma Phys. Control. Fusion **38**, 243 (1996).

[6] D. Dickinson, C. M. Roach, J. M. Skipp, and H. R. Wilson, Phys. Plasmas **21**, 010702 (2014).

[7] P. A. Abdoul, D. Dickinson, C. M. Roach, and H. R. Wilson, Plasma Phys. Control. Fusion **57**, 065004 (2015).

[8] A. Zocco, G. G. Plunk, P. Xanthopoulos, and P. Helander, Phys. Plasmas **23**, 082516 (2016).

[9] C. Kittel, *Introduction to Solid State Physics*, 4th ed. (John Wiley and Sons, 2005) Chap. 1.

[10] G. G. Plunk, P. Helander, P. Xanthopoulos, and J. W. Connor, Phys. Plasmas **21**, 032112 (2014).

[11] F. Romanelli, Phys. Fluids B **1**, 1018 (1989).

[12] R. L. Dewar and A. H. Glasser, The Phys. of Fluids **26**, 3038 (1983).

[13] W. A. Cooper, D. B. Singleton, and R. L. Dewar, Phys. Plasmas **3**, 275 (1996).

[14] M. Nunami, T.-H. Watanabe, and H. Sugama, Plasma Fus. Research **5**, 016 (2010).

[15] F. Jenko, W. Dorland, M. Kotschenreuther, and B. N. Rogers, Phys. Plasmas **7**, 1904 (2000).

[16] P. Xanthopoulos, H. E. Mynick, P. Helander, Y. Turkin, G. G. Plunk, F. Jenko, T. Görler, D. Told, T. Bird, and J. H. E. Proll, Phys. Rev. Lett. **113**, 155001 (2014).

[17] N. W. McLachlan, *Theory and Application of Mathieu Functions* (Oxford University Press, 1947).

[18] Formally, this is true for $m\rho_* \ll 2\left(\tau L_T/L_B\right)^{1/4}$

Appendix A: Derivation of Equation (6)

In Eq. (5), we introduce

$$\varphi(y) = \sum_n \varphi_n e^{iny}, \tag{A1}$$

and obtain

$$\begin{aligned}\sum_n \left[\tau - \frac{v_{thi} n^3 \rho_*^3}{4 L_T \omega}\right] \varphi_n e^{iny} = -\frac{v_{thi}^2}{\omega^2 L_B L_T} \Bigg\{ 1 + \frac{\epsilon_h f_M^c}{2} \left[e^{iNy} + e^{-iNy}\right] \\ + \frac{\epsilon_h f_M^s}{2i} \left[e^{iNy} - e^{-iNy}\right] \Bigg\} \sum_n \rho_*^2 n^2 \varphi_n e^{iny}.\end{aligned} \tag{A2}$$

Now, we project Eq. (30) onto the basis functions with the integral

$$\frac{1}{2\pi} \int_{-\pi}^{\pi} dy e^{-imy}, \tag{A3}$$

and get

$$\sum_n \int_{-\pi}^{\pi} dy \left[\tau - \frac{v_{thi} n^3 \rho_*^3}{4 L_T \omega}\right] \varphi_n e^{i(n-m)y} = -\frac{v_{thi}^2}{\omega^2 L_B L_T} \int_{-\pi}^{\pi} dy \sum_n \rho_*^2 n^2 \varphi_n e^{i(n-m)y}$$
$$- \frac{v_{thi}^2}{\omega^2 L_B L_T} \frac{\epsilon_h f_N^c}{2} \int_{-\pi}^{\pi} dy \sum_n \rho_*^2 n^2 \left[e^{i(N+n-m)y} + e^{-i(N-n+m)y}\right] \varphi_n \tag{A4}$$
$$- \frac{v_{thi}^2}{\omega^2 L_B L_T} \frac{\epsilon_h f_N^s}{2i} \int_{-\pi}^{\pi} dy \sum_n \rho_*^2 n^2 \left[e^{i(N-n-m)y} - e^{-i(N-n+m)y}\right] \varphi_n.$$

We use the identity

$$\delta_{n,l} = \frac{1}{2\pi} \int_{-\pi}^{\pi} dy e^{i(n-l)y}, \tag{A5}$$

and obtain Eq. (6).

Appendix B: A new class of functions

Our fundamental equation with no FLR

$$\hat{\omega}^2 \varphi(y) = -\left\{1 + \epsilon_h \cos y\right\} \left(-i\rho_* \partial_y\right)^2 \varphi(y). \tag{B1}$$

shares many features with the Mathieu equation. It is worth following a standard procedure [17] to construct a new class of functions which solve for it.

We know that, for $\epsilon_h = 0$, the solutions of Eq. (B1) are

$$\varphi(y) = \cos\left(\frac{\hat{\gamma}}{\rho_*} y\right), \tag{B2}$$

with $\hat{\gamma} = \Im[\hat{\omega}] = \rho_* m$, with m and integer. We are considering even solutions, however, a similar treatment is possible also for odd solutions. We now write

$$\frac{\hat{\gamma}}{\rho_*} = m^2 + \alpha_1 \epsilon_h + \alpha_2 \epsilon_h^2 + \ldots, \tag{B3}$$

and

$$\varphi(y) = \cos(my) + \epsilon_h c_{1,m}(y) + \epsilon_h^2 c_{2,m}(y) + \ldots \tag{B4}$$

We want to construct periodic solutions by using Eqs. (B3)-(B4) in Eq. (B1) and choosing the constants α_i to annihilate secular terms. It is easy to check that

$$c_{1,m}(y) = \frac{m^2}{4m^2 - 1} \left\{\cos(my) \cos y - 2m \sin(my) \sin y\right\} \tag{B5}$$

where

$$\alpha_1 = 0, \tag{B6}$$

and

$$c_{2,m}(y) = \frac{m^2}{8}\frac{1}{4m^2-1}\left\{\left(2m^2-1\right)\cos(2y)\cos(my) - 2m\cos y \sin y \sin(my)\right\}, \tag{B7}$$

where

$$\alpha_2 = \frac{m^2}{2}\frac{1-3m^2}{4m^2-1}, \tag{B8}$$

and so on. Notice that for $m \gg 1$ we obtain, in yet another way, the stabilizing second order correction to the eigenvalue already derived in Eq. (53) of Ref. [8]. The new special functions are plotted in Fig. (15) for a low $m : m = 4$. For a higher value of $m : m = 20$, their typical behavior is plotted in Figs. (16)-(18).

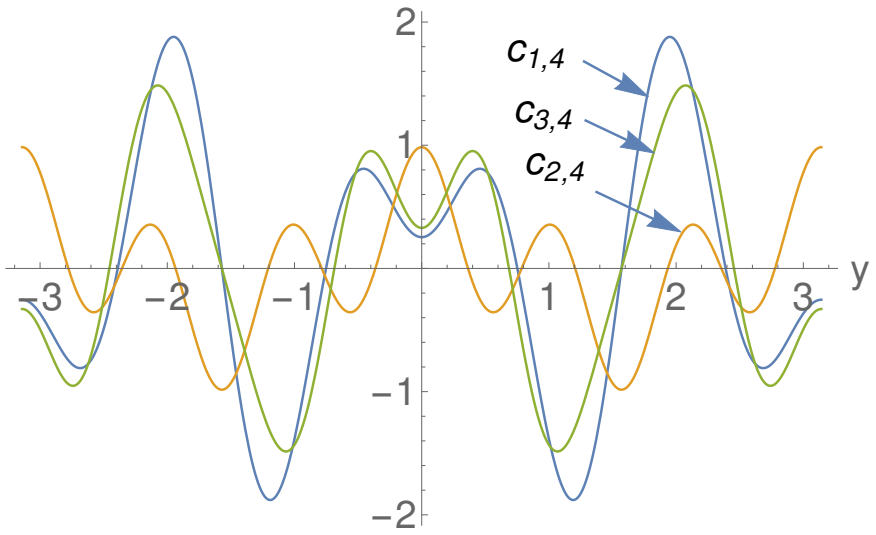

Figure 15: For $m = 4$.

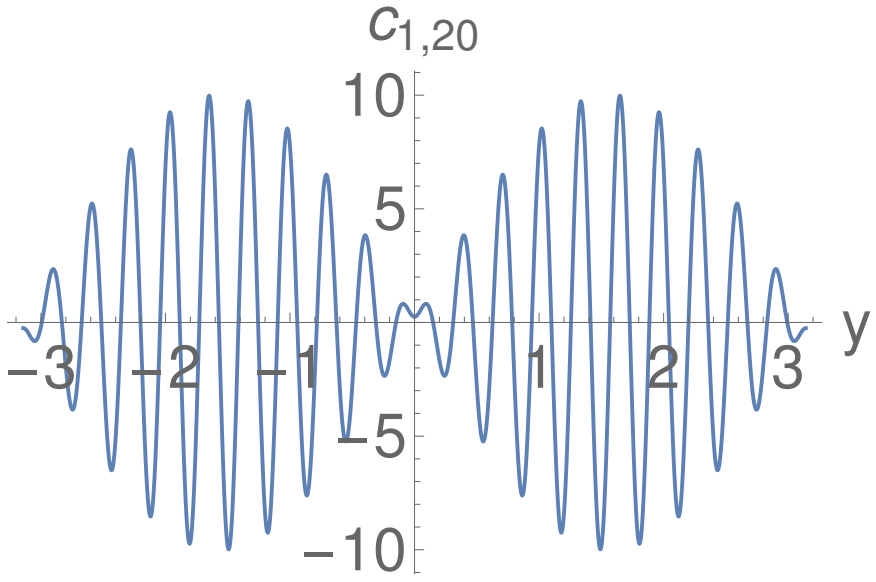

Figure 16: The function $c_{1,20}$

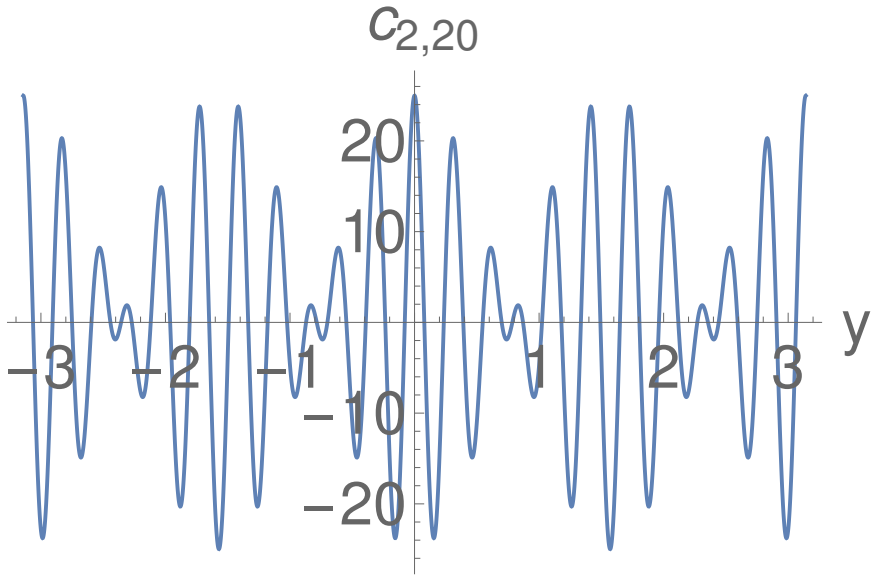

Figure 17: The function $c_{2,20}$

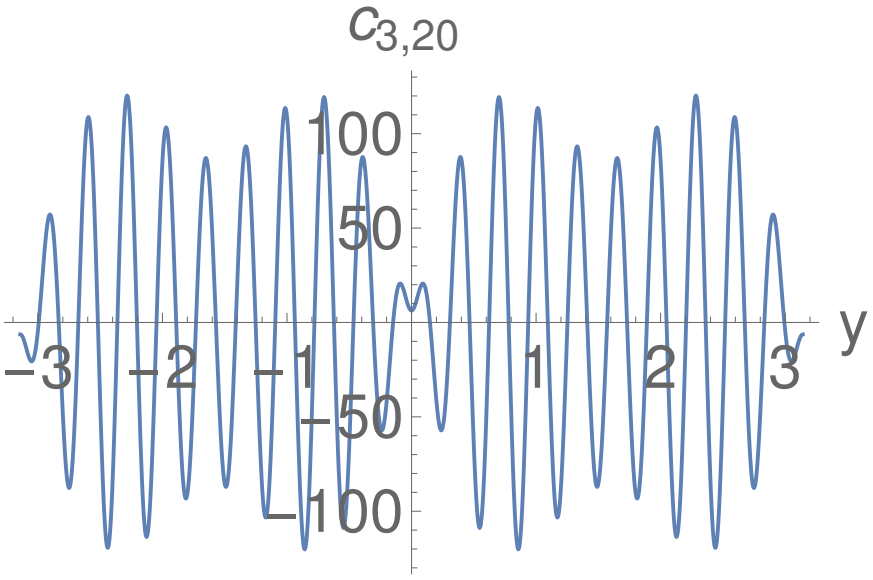

Figure 18: The function $c_{3,20}$